Aeroacoustic effect of boundary layer separation control by rod vortex generators on the DU96-W-180 airfoil

Suresh, Thanushree; Flaszynski, Pawel; Carpio, Alejandro Rubio; Kurowski, Marcin; Piotrowicz, Michal; Szulc, Oskar

DOI
10.1016/j.jfluidstructs.2024.104133

Publication date
2024

Document Version
Final published version

Published in
Journal of Fluids and Structures

Journal of Fluids and Structures 127 (2024) 104133

Contents lists available at ScienceDirect

Journal of Fluids and Structures

journal homepage: www.elsevier.com/locate/jfs

Aeroacoustic effect of boundary layer separation control by rod vortex generators on the DU96-W-180 airfoil

Thanushree Suresh [a,*], Pawel Flaszynski [a], Alejandro Rubio Carpio [b], Marcin Kurowski [a], Michal Piotrowicz [a], Oskar Szulc [a]

[a] Institute of Fluid-Flow Machinery, Polish Academy of Sciences, Fiszera 14, Gdansk, 80-231, Poland
[b] Delft University of Technology, Mekelweg 5, Delft, 2628, Netherlands

ARTICLE INFO

Keywords:
Wind energy
Noise emissions
Acoustic beamforming
Particle image velocimetry

ABSTRACT

An experimental campaign to study the impact of a distinct type of vortex generator — rod type (RVG), on the flow characteristics and the acoustic far-field pressure of a wind turbine airfoil, is conducted. Airfoils exhibit decreased aerodynamic performance at high inflow angles due to turbulent boundary layer flow separation. RVGs are applied to mitigate the flow separation. However, this benefit is accompanied by an acoustic penalty. An assessment of the impact of RVGs on the far-field noise emission is conducted for the DU96-W-180 airfoil. The evolution of the boundary layer impacted by the rods is analyzed through Particle Image Velocimetry (PIV) measurements. The resulting reduction in the separation zone is observed through oil flow visualization. Analysis of the sound spectrum for airfoils with/without RVGs is conducted for a range of frequencies (300 Hz to 4000 Hz). Results show a reduction of the noise level at relatively low frequencies, at the expense of an increased noise level in the mid-high frequency ranges. While the former is caused by the reduction of the flow separation, the latter is determined by the combined contribution of the noise scattered by the RVG and by the change in boundary layer characteristics at the airfoil trailing edge.

1. Introduction

Wind energy is one of the promising sources of renewable energy to meet our exponentially growing energy demands. With the rising number of wind farms, there has also been a simultaneous increase in the public's annoyance with onshore wind farms, specifically due to noise emissions (Doolan, 2013). Societal concerns have forced policymakers and governments to impose stringent noise regulations on wind farms in the vicinity of populated areas (Davies et al., 2015). Sound levels emitted by wind turbines increase proportionally to the 5-6th power of the tip speeds (Oerlemans et al., 2007). To satisfy the imposed noise regulations, wind turbines are often forced to operate at reduced capacities, driving up energy costs.

Numerous flow and acoustic analyses have been conducted for wind turbine blades operating at design conditions (Hanning and Evans, 2012; Avallone et al., 2018; Bowdler et al., 2012; Cao et al., 2020) and their predominant turbulent boundary layer trailing edge noise (Blake and Gershfeld, 1989; Oerlemans et al., 2009; Carpio et al., 2018; Garcia-Sagrado and Hynes, 2012). At off-design conditions, they experience adverse pressure gradients. This causes boundary layer separation leading to aerodynamic losses, stall, and fatigue loads (Gad-el Hak and Bushnell, 1991; De Tavernier et al., 2021), all of which, reduce performance thereby increasing energy costs. With time, degradation of the blade surface (causing roughness), leading edge erosion, etc. also impact boundary layer properties thus inducing local flow separation (Latoufis et al., 2019; Sareen et al., 2014).

* Corresponding author.
E-mail address: thanu@imp.gda.pl (T. Suresh).

https://doi.org/10.1016/j.jfluidstructs.2024.104133
Received 31 October 2023; Received in revised form 30 April 2024; Accepted 7 May 2024
Available online 24 May 2024

Several active and passive flow control devices (Chen and Wen, 2021; Siozos-Rousoulis et al., 2017; Greenblatt et al., 2012) including vortex generators (Kösters and Hoerner, 2023; Lin, 2002; Monir et al., 2014; Pauley and Eaton, 1988; Bons et al., 2000) have been implemented in various applications for differing operating conditions to tackle the problem of flow separation. Vortex Generators (VGs) are designed to suppress/delay flow separation by re-energizing the boundary layer, enhancing mixing with streamwise vortices along the blade surface (Szwaba et al., 2019; Gao et al., 2015). Limited studies focussing particularly on the acoustic impact of VGs (vane-type) are available (Ye et al., 2020; Kolkman et al., 2018).

A specific type of streamwise VG, called the Rod Vortex Generator (RVG) was investigated for the reduction of boundary layer separation (Szwaba et al., 2019; Flaszynski et al., 2016). Similar to the vane VG or Air-jet type vortex generators (AJVGs), RVGs create streamwise vortices due to the interaction of the inclined rod with boundary layer flow. The advantage of the designed RVGs compared to AJVGs is that they generate streamwise vortices faster (Tejero Embuena et al., 2018) and in some cases, the implementation on complex applications like helicopter rotor blades is easier (Tejero et al., 2015). Additionally, these rods have an advantage over classical vane types as they can be easily activated only at the off-design conditions by utilizing micro-electro-mechanical systems (MEMS) technology (Lewandowski, 2017). This feature would allow for more flexibility in implementing blade add-ons thus aiding the trade-off between separation reduction and aerodynamic performance.

RVGs have been studied for various applications (Suarez et al., 2018a,b; Doerffer, 2014), specifically, for separation reduction and improved aerodynamic performance. It is not yet clear whether the increased performance due to the employment of RVGs is counteracted by the change in acoustic emissions. The self-noise sources of sound in airfoils are a function of the characteristics of the boundary layer, which are affected by the add-ons (VGs). Considering the previous studies proving the aerodynamic capability of the RVGs to operate in different flow regimes — subsonic and transonic applications, MEMS technology adaption benefits, the state-of-art question is their acoustic impact. Given the main environmental concerns of the society regarding noise levels especially for wind energy, research into how the RVGs influence the sound levels emitted by the wind turbine rotors becomes important. This is the main objective of the current paper. The acoustic impact of vortex generators is limited in literature and specifically the rod type of VGs is unknown.

The present study is conducted to update this missing information (acoustic impact) regarding the RVGs. With the implementation of the rods, the separation zone is reduced and consequently, a reduction in separation noise is expected (Suarez et al., 2018b). RVGs achieve this by re-energizing the boundary layer through a transfer of momentum from the outer regions of the flow to close to the wall. This generates more turbulent kinetic energy and thus increases pressure fluctuations close to the wall (Lin, 2002). Thereby, an increase in the turbulent trailing edge noise is anticipated (Kolkman et al., 2018). The overall effect on the emitted sound levels by the RVGs, given the above-mentioned primary competing noise mechanisms is still unclear. Additionally, self-noise due to the rod surfaces can be expected at certain frequencies (Kolkman et al., 2018). To study this, measurements are conducted on a wind turbine airfoil DU96-W-180, both, with/without RVGs, and presented in this paper. To further analyze the impact of the rods on the flow structures in the separation zone, oil flow visualization and Particle Image Velocimetry (PIV) measurements are conducted. Analysis of the sound pressure levels of the airfoil with/without flow control is performed through acoustic measurements using a microphone array. The first Section of the paper introduces the background and motivation behind this research work. The theoretical background and methodology are detailed in Section 2. The impact of the RVGs on the flow characteristics are presented in Section 3 followed by the effect of the rods on the acoustic emission of the airfoil in Section 4. The main findings and conclusions of this research undertaking are summarized in the last Section.

2. Experimental set-up and measurement techniques

Experiments are conducted in the anechoic, vertical, open-jet wind tunnel (A-tunnel) in the Low-Speed Laboratories at Delft University of Technology (TUD). The influence of a range of inflow angles on the flow structure and acoustics generated by the rods on a wind turbine airfoil (DU96-W-180) is investigated. The DU96-W-180 airfoil is particularly chosen since it is an airfoil that was designed for wind turbine applications (Timmer and Van Rooij, 2003) and data exists in the literature for a similar open-jet wind tunnel (Suryadi and Herr, 2015) that aided the validation of the design strategy. Measurements are conducted in the rectangular test section of dimensions $0.4\,\mathrm{m} \times 0.7\,\mathrm{m}$ and a contraction ratio of 15:1 (Fig. 1). The flow velocity is $30\,\mathrm{m/s}$ with turbulence intensity of 0.1%. Further characteristics of the wind tunnel are available in Merino-Martinez et al. (2020). The airfoil is held between two side plates of $1.2\,\mathrm{m}$ length and is at a distance of $0.5\,\mathrm{m}$ from the nozzle exit.

2.1. Design of the airfoil model and RVGs

The airfoil and the RVG dimensions are designed using numerical simulations before manufacturing. The computational model used in the design process was validated against an existing experimental campaign that was conducted by Suryadi and Herr (2015). This particular data was chosen from the literature due to the similar open-jet test section configuration and the same DU96-W-180 airfoil. The validated numerical model for the reference airfoil (airfoil without RVGs) was then extended to include the test section constraints of the TUD's A-tunnel where the experimental campaign is conducted.

Using the boundary layer characteristics estimated from the numerical simulations, the dimensions and parameters of the RVGs are designed based on the optimum design ratios that were obtained from previous studies (Suarez et al., 2018b; Flaszyński and Szwaba, 2008). A parametric study of the RVG design variables specifically for the wind turbine application was conducted by Suarez et al. (2018a). Studies showed that for efficient flow control, the geometric parameters should be proportional to the developed boundary layer thickness (δ). RVGs are characterized by four parameters: diameter (D), height (h), skew angle (ϕ), and pitch angle

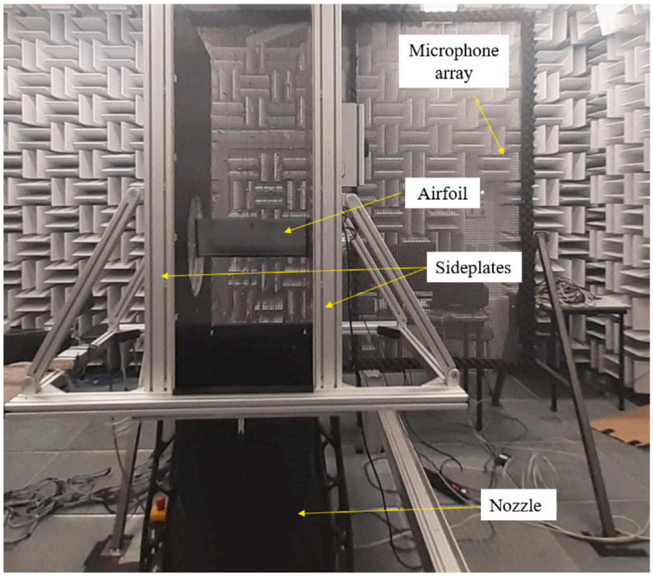

Fig. 1. Anechoic, vertical open-jet test section at TUD with DU96-W-180 airfoil.

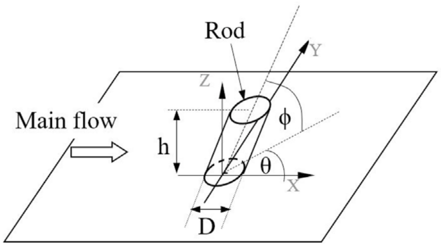

Fig. 2. A single RVG.

(θ) as seen in Fig. 2. Their implementation depends on the spanwise distance between the rods (W) and the relative chordwise location (x_{RVG}/c). Suarez performed three-dimensional Reynolds-Averaged Navier–Stokes (RANS) simulations for a single rod on a flat plate for different Reynolds numbers and a range of angles of attack. This numerical model was validated with measurements conducted for a rod with $\theta = 90°$, $\phi = 45°$, $\delta = 10\,\text{mm}$, $D/\delta = 0.2$ and $h/\delta = 0.36$. Aerodynamic performance indicators such as pressure distribution (C_p), evolution of boundary layer profiles, and visualization of vortices using contours of stagnation pressure from numerical simulations were in good agreement with measurements.

Using the validated numerical model, a parametric study of the dimensions of the rods was conducted for a range of angles. It was found that $\theta = 30°$, $\phi = 45°$ are the optimum values. Similarly a range of ratios for diameter (D/δ) – 0.2, 0.28, 0.48, 0.8, 1 and height (h/δ) – 0.2, 0.32, 0.36, 0.4 were conducted to evaluate their influence on streamwise vorticity and circulation. Analysis shows that the ratios $D/\delta = 0.2$ and $h/\delta = 0.36$ were found to be optimum (Suarez et al., 2018b) similar to previous analysis conducted within the research group (Flaszyński and Szwaba, 2008). Studies for the chordwise location of the rods were performed for a range of $x_{RVG}/c = 0.35, 0.4, 0.45, 0.5, 0.55$ at high inflow angles with flow separation. Contour maps of skin friction coefficient, lift, and drag coefficients were analyzed and show that the mid-chord location is optimum ($x_{RVG}/c = 0.5$). Similar studies were conducted for the spanwise location of the rods placed at the mid-chord location. Rods placed at $W/D = 7.5$, 10, 15, 20 were analyzed and results show that $W/D = 10$ is the optimum configuration (Suarez et al., 2018b).

Based on these studies and utilizing the upstream boundary layer thickness estimated from the preliminary numerical simulations, the airfoil and RVGs were manufactured for the experimental campaign. The geometric characteristics of the rods are presented in Table 1.

Typically the airfoils are made of composite materials but in the present study, the airfoil is made of a homogeneous material — aluminium alloy. This is because the airfoil is equipped with an interchangeable metal insert that contains the rod vortex generators (Fig. 3). This allows for implementing various inserts with different characteristics of the rods for future studies. The airfoil was manufactured using a Computer Numerical Controlled (CNC) machine with an alloy of aluminium since the material does not affect the flow structures. Measurements are conducted for clean airfoils (reference and flow controlled) and airfoils with a zig-zag trip (reference and flow controlled) of 12 mm width and 0.6 mm height placed at 5% chord from the leading edge on the suction side and at 10% chord on the pressure side (Suryadi and Herr, 2015).

Table 1
Airfoil and RVG design parameters.

Airfoil material	Aluminium alloy
Airfoil span (s)	0.4 m
Airfoil chord (c)	0.15 m
RVG material	steel
RVG height (h)	2 mm
RVG diameter (D)	0.8 mm
RVG skew angle (ϕ)	30°
RVG pitch angle (θ)	45°
Number of rods	44
RVG chordwise location (x_{RVG}/c)	0.5
Distance between the rods (W)	8 mm

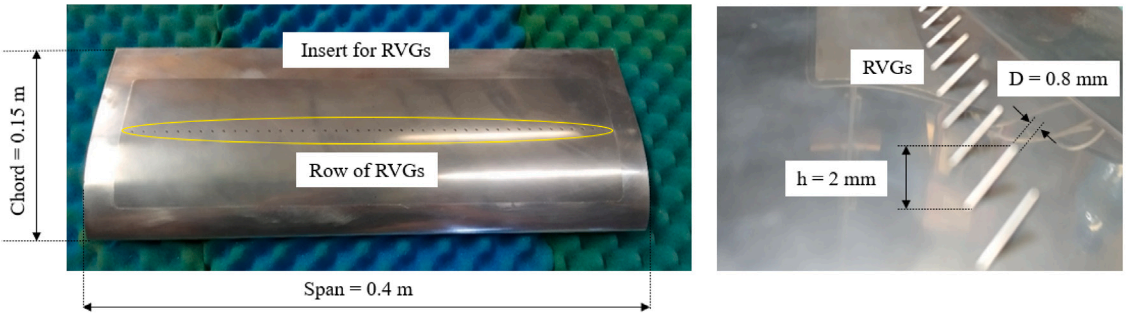

Fig. 3. DU96-W-180 airfoil with interchangeable insert for RVGs.

2.2. Flow measurements

The surface pressure distribution on the airfoil is estimated through pressure measurements. The impact of the RVGs on the flow structures and the separation zone reduction is characterized by oil flow visualization. Additionally, the re-energizing of the boundary layer by the streamwise vortices generated by the rods is assessed through PIV measurements.

Surface pressure measurements were obtained for a range of angles of attack from −4° to 20° (steps of 2°) using Honeywell TruStability transducers (range: −6 kPa to 6 kPa, uncertainty: 12.5 Pa). Pressure taps are located in the midspan of the airfoil at a distance of 10 mm from each other (chordwise) on the suction side. The first pressure tap is located at $x/c = 0.16$ and the last tap at $x/c = 0.9$ with ten taps placed in-between. Differential pressure obtained from the transducers is used to compute the pressure coefficient (C_p) using Eq. (1) where Δp is the measured differential pressure, ρ is the measured density and U_∞ is the flow velocity (Abbott and Von Doenhoff, 2012).

$$\Delta C_p = \frac{\Delta p}{0.5\rho U_\infty^2} \tag{1}$$

Oil flow visualization is conducted by painting the suction side of the airfoil surface using a fluorescent mixture obtained from 50 mL liquid-paraffin wax and 15–25 drops of fluorescent oil additive A-680. The flow over the airfoil is set to the operating conditions and allowed to develop for a few minutes, so the paraffin is scattered over the entire airfoil surface. The airfoil is then illuminated by an ultraviolet lamp with a wide aperture, positioned perpendicular to the model and then the resulting images are obtained.

Two-dimensional PIV measurements are conducted at the mid-chord of the airfoil, both with/without RVGs to investigate the effect of generated streamwise vortices on velocity profiles in a boundary layer. The velocity measurements are obtained at three planes in the X–Z direction, located at the base (plane 1), middle (plane 2), and top (plane 3) of a single rod (Fig. 4). Each plane is separated by a distance of 2.5 mm. The laser beam is obtained from a Quantel EverGreen EVG00200 system with a wavelength of 532 nm and energy of 20 mJ/pulse. Seeding is provided by a SAFEX Twin-Fog double-power fog generator using glycol based solution. Two cameras: LaVision VC-Imager Pro LX (4870 × 3246 pixel^2, 12 bits, 7.4 micron/px) are located at a distance of 0.16 m from the measurement planes. Both cameras are equipped with Nikon AF Micro Nikkor 200 mm focal distance lenses. To offset bias errors due to peak-locking, the images are slightly defocused resulting in a particle image larger than 2 pixels (Westerweel, 1997). LaVision high-speed controller is utilized for laser beam illumination and image acquisition. The sampling frequency for the data is 1 Hz. The field of view is $0.28c \times 0.19c$ (42 × 29 mm^2) with a digital resolution of 0.1 px/mm. The post-processing of the data is conducted in LaVision DaVis 8.4 software using a multi-pass cross-correlation algorithm with window deformation (Scarano, 2001). The final interrogation window size is 16 × 16 pixel^2 with an overlap factor of 50% resulting in a spatial resolution of 0.14 mm and a vector spacing of 0.2 mm.

Measurement errors due to sources of uncertainty, calibration, and lens distortion are mitigated with a self-calibration process within the DaVis software. The uncertainties in the measurement is evaluated using the Wieneke method (Wieneke, 2015). The

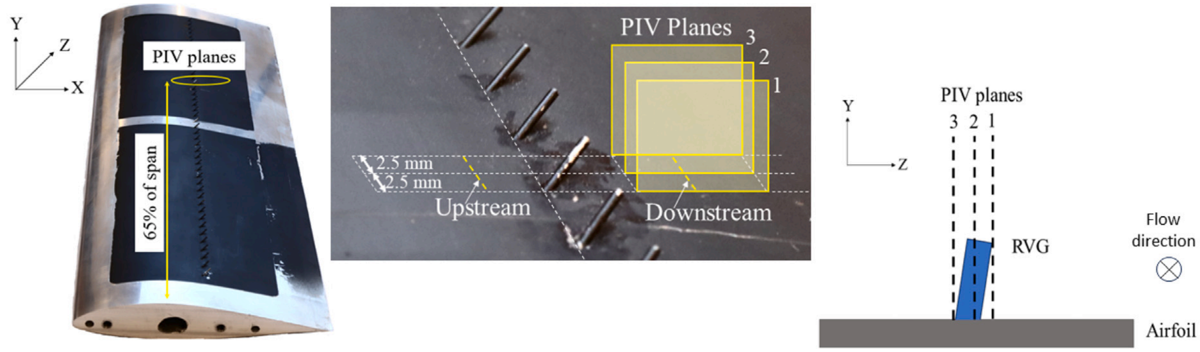

Fig. 4. PIV field of view details.

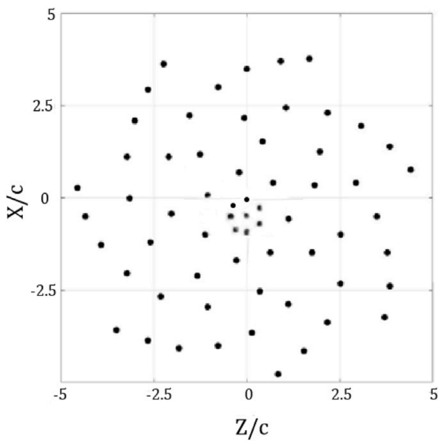

Fig. 5. Adapted Underbrink design (Carpio et al., 2019).

uncertainty on the mean freestream velocity (U_∞) and on the root-mean-square velocity ($\sqrt{\overline{u^2}}$) with a 95% confidence level are $0.02U_\infty$ and $0.04\sqrt{\overline{u^2}}$ respectively computed using the method described in Carpio et al. (2019).

2.3. Acoustic measurements

The influence of the RVGs on the trailing edge noise and the overall noise levels emitted by the airfoil is assessed for a range of frequencies through acoustic measurements. Measurements are conducted using a phased array of 64 free-field microphones (G. R. A. S. 40 PH) with a frequency range of 10 Hz–20 kHz (±1 dB), maximum output of 135 dB (reference pressure of 2×10^{-5} Pa), with integrated constant current power (CCP) pre-amplifiers is implemented. The microphones are arranged in an adapted Underbrink design (Underbrink, 2001; Prime and Doolan, 2013) with 7 spiral arms of 9 microphones each as seen in Fig. 5 with one microphone at the center of the array. The diameter of the array is 2 m and the distance from the center of the array to the airfoil at angle of attack, AoA = 0° is 1 m. The trailing edge of the airfoil is 15 cm below the center microphone. The microphone array has a sampling frequency of 51 kHz and a recording time of 20 s.

Conventional frequency domain beamforming (CBF) is applied to the measured acoustic data to identify noise sources (Allen et al., 2002; Oerlemans, 2009). The airfoil acts as the scan plane defined by the grid points which are each assumed to be potential sound sources whose power is to be computed (Santana, 2017). Applying Fourier transform and windowing using a Hanning weighting function with 50% data overlap (Welch, 1967) the cross-spectral matrix (CSM) is obtained. Using steering vectors, the source power at every grid point on the scan plane is obtained with an accuracy of 1 dB (Martinez et al., 2020). The scan grid plane is of the range $-0.35 < z < 0.35$ and $-0.25 < x < 0.25$ where z-coordinate denotes the spanwise direction and x-coordinate denotes the chordwise direction. The minimum distance between the two sources ($\triangle l$) that can be resolved is governed by the Rayleigh criterion (Lord Rayleigh, 1879) (Eq. (2))

$$\triangle l \approx 1.22 h_s \frac{c_o}{f D_a} = 1.22 h_s \frac{\lambda}{D_a}. \tag{2}$$

With distance to the scan plane (h_s) being 1 m, c_o as the speed of sound in m/s, λ as acoustic wavelength in m, and array aperture (D_a) of 2 m, this microphone array has a Rayleigh resolution range of 2.12 m to 0.01 m for the corresponding frequency (f) range of

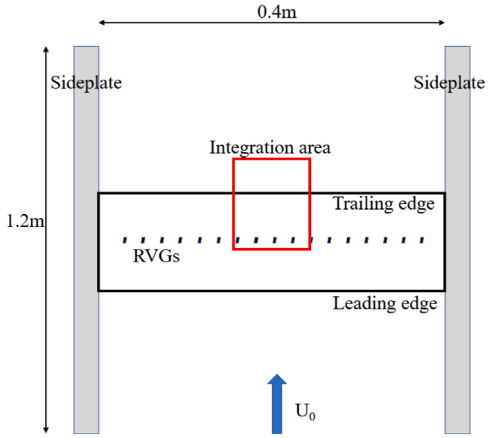

Fig. 6. Region of interest (ROI).

100 Hz to 20 000 Hz. A comparison of the spectral analysis (SPL — Sound Pressure Levels, OASPL — Overall Sound Pressure Levels) for the flow controlled airfoil (equipped with RVGs) against the reference airfoil is conducted for a range of frequencies. The SPL is computed using Eq. (3) where p is the root mean square of pressure fluctuations, and p_0 is reference pressure (2×10^{-5} Pa) (Sijtsma, 2010)

$$SPL = 10 \log_{10} \left(\frac{p^2}{p_0^2} \right). \tag{3}$$

Due to the tunnel cut-off, spectral analysis is conducted from 300 Hz to 4000 Hz. However, the rods' self-noise is observed only at contour maps of much higher frequencies (~5000 Hz to 7000 Hz) presented in Fig. 20. Additionally, only the difference in SPL between the flow controlled and reference case is plotted to reduce the impact of background noise at higher frequencies. For analyzing the impact of RVGs, the sound pressure levels are obtained by integrating the specific region of interest (ROI) (Brooks and Humphreys, 1999), $0.38 < z/s < 0.63$ and $0.47 < x/c < 1.4$ presented in Fig. 6. All presented spectra are in one-third-octave bands.

To identify some of the weak secondary sources such as the rods, the High Resolution CleanSC deconvolution method is applied (Sarradj, 2010; Luesutthiviboon et al., 2018; Sijtsma et al., 2017). This method removes the side lobes due to the dominant noise sources, from the CSM matrix, in an iterative process to clean up the source map. Further details on the particular beamforming procedure used in this paper can be found in Luesutthiviboon et al. (2019). Since the microphone array is in a stationary medium while the acoustic source (airfoil) is located in the flow, a correction factor is needed for the source location (Padois et al., 2013). A correction of $x = 0.05$ m obtained from $x = Mw_f$, where $M = 0.086$ is the Mach number and $w_f = 0.5$ is the distance of the source from the shear layers (Luesutthiviboon et al., 2019) is incorporated.

3. RVG effect on separation reduction

In this section, analysis of the data obtained from the flow measurement techniques such as surface pressure, oil flow visualization, and PIV are presented. The distribution of pressure on the suction side of the airfoil is measured through the pressure taps installed at mid-span. The measured pressure for the reference case airfoil is presented in Fig. 7 for the geometric angle of 0°. The measured data is compared with the XFOIL code predictions to correct for open-jet effects to estimate the correction angle. This correction angle grows linearly with increasing inflow angles and is within a range of 0°–1° for geometric angles in the linear region of flow. The angles mentioned henceforth in the paper are all effective inflow angles.

The impact of the RVGs on the separation reduction is observed through oil flow visualization. The characteristics of the flow for the airfoil at an angle where a sufficiently large separation zone is developed (effective AoA = 6°) are presented in Fig. 8. The freestream velocity is denoted as "A" in the figures. A large zone of turbulent flow separation occurs at the mid-chord extending up to the trailing edge. In the separation zone, the oil is unable to be transported by shear stresses and begins to accumulate. Further downstream the flow is completely separated. Oil moving from the leading edge towards the mid-chord represents the vortices that are generated by the trip tape (E). Corner vortices that are generated due to the interaction of the flow with the boundary layers at the region where the airfoil is mounted on the side plates (Gardner and Richter, 2013), are denoted as "B". The flow is almost uniform in the spanwise direction. The flow separation line is denoted as "C". A second row of cell like structures that are visible are the traces of streamwise vortices generated by the rods in the low shear stress regions where the oil is not fully washed away. At the corner zone, a very small asymmetry is observed which may arise from small differences in the incoming flow at the sidewall and airfoil junction. With increasing inflow angle, a turbulent separation zone (which starts close to the trailing edge) develops and moves towards the leading edge. Streaks of oil starting at mid-chord and moving towards the trailing edge characterize the vortices

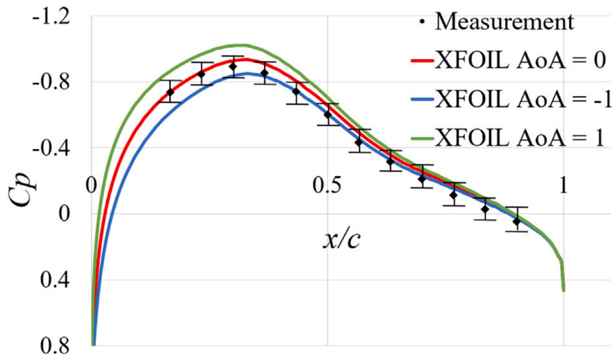

Fig. 7. Pressure coefficient (C_p) comparison for the DU96-W-180 airfoil. (For interpretation of the references to color in this figure legend, the reader is referred to the web version of this article.)

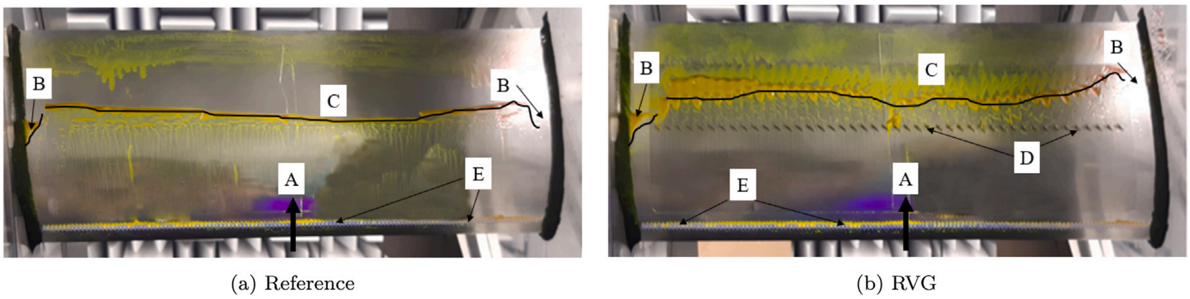

Fig. 8. Oil flow visualization for DU96-W-180 airfoil at AoA = 6°.

Table 2
Normalized turbulent separation zone comparison.

Configuration	Reference	RVG	Reduction (%)
AoA = 6°	0.26	0.20	23

generated by the rods. These streamwise vortices energize the flow, keeping them attached to the surface longer, thus shifting the separation line (C) towards the trailing edge. Additionally, rods are inclined towards the left sidewall, and these vortices are generated as co-rotating vortices, thus they introduce an asymmetry in the flow structure. This effect is clearly visible in Fig. 8b marked as “B”.

The effectiveness of the rods in reducing the separation zone has been presented in the analysis of Fig. 8. This is further supported by the numerical estimation presented in Table 2. It consists of the ratio of the turbulent separation area normalized with the suction side area. The rods reduce the separation zone by ∼23%.

The evolution of the boundary layer velocities is analyzed through the measured PIV data. The mean streamwise velocity profile at the upstream location ($x/c = 0.43$) for the reference airfoil is plotted in Fig. 9, where, the non-dimensionalized velocity given by $u^+ = u/u_\tau$ and wall coordinate is given by $y^+ = yu_\tau/\nu$ (ν is the kinematic viscosity) (Clauser, 1956). The profile is scaled using the friction velocity $u_\tau = \sqrt{\tau_w/\rho}$ (with τ_w being wall shear stress and ρ is the fluid density) to fit the theoretical boundary layer in the buffer and the logarithmic region. The value of u_τ is obtained through an iterative fitting of the measured data with the log law equation characterized by the universal constants $\kappa = 0.41$ and $B = 5.1$ (Clauser, 1956). Only the measurements fitting the law are utilized for further analysis.

Velocity curves for both the reference and flow controlled airfoils at AoA = 6° are analyzed below. Various velocity components at two streamwise locations — one before the onset of the separation at $x/c = 0.43$ (upstream) and one inside the separation zone at $x/c = 0.63$ (downstream) are plotted. A comparison of the reference and the flow controlled velocity curves is conducted to observe the impact of the rods on the evolution of the boundary layer. The velocity is normalized by the freestream velocity (U_∞) and the wall-normal distance by the boundary layer thickness (δ_{99}).

The mean streamwise velocity curve for the reference airfoil upstream of the rods ($x/c = 0.43$) is presented in Fig. 10. Here, the data from only one plane is presented because the velocity curves at all the other planes are similar. This is due to the flow being uniform in the spanwise direction at this location. The mean streamwise velocity profiles for the RVG case are compared with the reference, far downstream of the rods (Fig. 10). The variations in the velocity due to the vortical structures generated by the rods are visible in the plane 2 (red line) and plane 3 (green line) curves. The difference in the streamwise velocity distribution is dependent

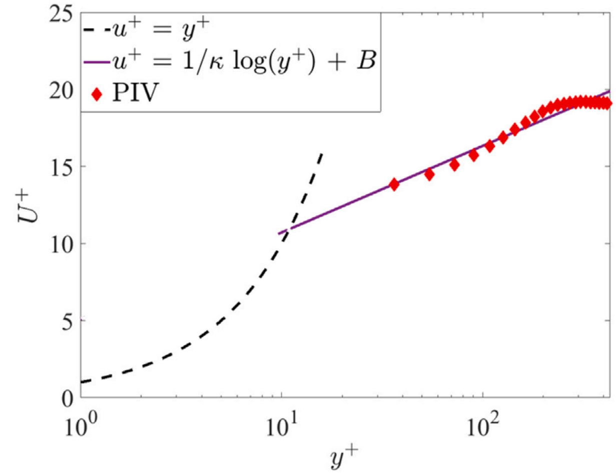

Fig. 9. Mean streamwise velocity profile with viscous scaling for reference airfoil at x/c = 0.43 (upstream) location.

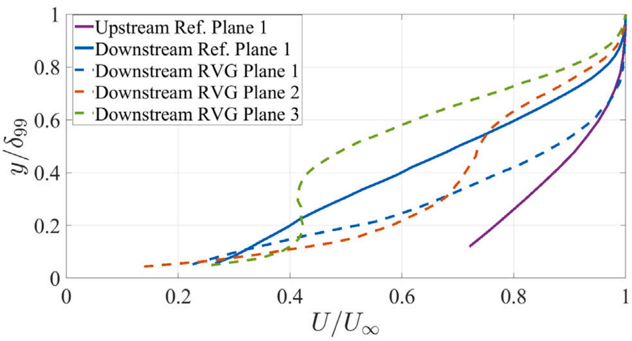

Fig. 10. Mean streamwise velocity component U/U_∞ at streamwise locations: x/c = 0.43 (upstream) and x/c = 0.63 (downstream). (For interpretation of the references to color in this figure legend, the reader is referred to the web version of this article.)

on the location of the velocity traverse in the zone of the vortex, in the spanwise direction. A similar effect has been presented for the streamwise vortices generated by jets in high-speed flow by Souverein and Debiève (2010). The spanwise modulation of the streamwise velocity component is observed at planes 2 and 3. At plane 2, the velocity is higher than in plane 1 up to y/δ_{99} = 0.3. Above this location, lower values than at plane 1 are observed. Furthermore, in the outer part of the boundary layer, the flow becomes uniform again. A more significant effect is observed at plane 3, where the velocity is even higher close to the wall (up to y/δ_{99} = 0.1), then decreases and finally reaches the same value as in plane 1 and 2, close to the limit of the boundary layer. The non-uniformity of the velocity components downstream of the rods is the effect of generated vortices and their existence in the boundary layer affects the structure of the separation line. This is a typical structure for the interaction of the streamwise vortices with the reversed flow downstream of the separation line. Although the velocity curves at the downstream location are in the separation zone (Fig. 8), it is not visible in the plots presented below. This is because the height of the separation zone is quite small and the measurements in this region (close to the wall surface) are not available as observed in Fig. 9.

The mean wall-normal velocity components at selected traverses upstream and downstream of the RVG are presented in Fig. 11. In the case of the reference airfoil, without RVGs, both curves (solid lines) show the same trend. The only difference is a lower magnitude of this velocity component farther downstream. A different distribution of the velocity curves is observed for the airfoil equipped with the rods due to the generated vortices operating in the boundary layer downstream of each rod (Suarez et al., 2018a). Curves representing neighboring traverses (planes 1–3) show spanwise non-uniformity of the velocity downstream of the RVGs. The negative velocity values indicate that the flow is directed towards the wall while the positive values indicate that the flow is moving away from the wall, an effect of the local rotation enforced by the vortex. Thus the streamwise vortex transports momentum from the outer region of the flow to the boundary layer, energizing it.

The boundary layer characteristics are computed for upstream and downstream locations and compared with the flow controlled airfoil in Table 3. The boundary layer thickness δ_{99} and the velocity $U_\infty = U(\delta_{99})$ are obtained from the velocity profiles. The boundary layer displacement thickness δ^*, momentum thickness θ and the shape factor H are also computed (Puzyrewski and Sawicki, 1987).

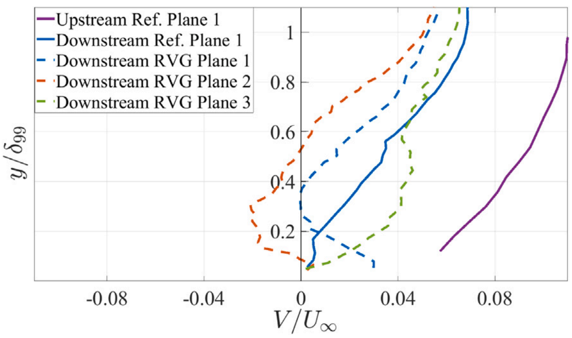

Fig. 11. Mean wall-normal velocity component V/U_∞ at streamwise locations: x/c = 0.43 (upstream) and x/c = 0.63 (downstream). (For interpretation of the references to color in this figure legend, the reader is referred to the web version of this article.)

Table 3
Boundary layer parameters at streamwise locations: $x/c = 0.43$ (upstream) and $x/c = 0.63$ (downstream).

	Upstream	Downstream			
	Plane 1	Plane 1		Plane 2	Plane 3
Parameters	Reference	Reference	RVG	RVG	RVG
U_∞ (m/s)	39.3	33.6	34	34.1	33.9
δ_{99} (mm)	2.4	5.1	5.4	6.5	5.9
$\delta *$ (mm)	0.3	1.6	1.2	1.8	2.4
θ (mm)	0.2	0.8	0.6	0.9	1.1
H	1.3	2.1	2.0	1.9	2.3

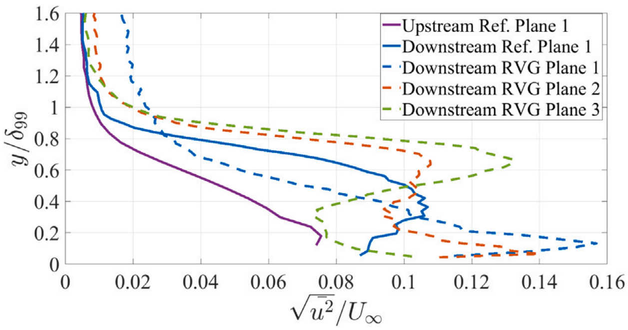

Fig. 12. R.m.s velocity component $\sqrt{\overline{u^2}}/U_\infty$ at streamwise locations: x/c = 0.43 (upstream) and x/c = 0.63 (downstream). (For interpretation of the references to color in this figure legend, the reader is referred to the web version of this article.)

The boundary layer thickness δ_{99} is higher for the RVGs when compared to the reference airfoil. Rods energize the flow within the boundary layer indicated by the increased velocity values at the three planes. The variation of the boundary layer thickness across the three planes indicate the presence of a streamwise vortex (Johnston et al., 2002).

The turbulent flow field i.e. root-mean-square velocity (r.m.s) at both the upstream and downstream locations for the wall-parallel velocity and the wall-normal velocity components are represented in Figs. 12 and 13 respectively.

Similar to the trends of the mean velocities discussed in the previous section, the fluctuations of the r.m.s velocity components increase at the downstream location compared to the upstream location. For the RVG case, there is an increase in the velocity fluctuations close to the wall indicating that the vortex (generated by the rods) energizes the flow.

4. RVG effect on acoustic sources

The impact of the streamwise vortices generated by the RVGs on reducing separation has been presented in the previous section. Given this, their impact on the overall sound generated by the airfoil is analyzed in this section. Broadband trailing edge noise observed on the SPL contour maps for the flow controlled airfoil is compared against the reference airfoil to analyze the impact of the streamwise vortices (RVGs) on the trailing edge noise.

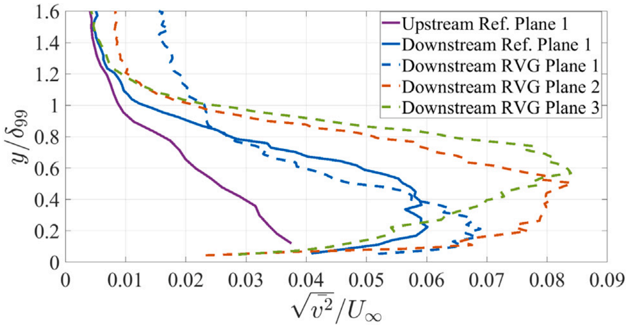

Fig. 13. R.m.s velocity component $\sqrt{v^2}/U_\infty$ at streamwise locations: x/c = 0.43 (upstream) and x/c = 0.63 (downstream). (For interpretation of the references to color in this figure legend, the reader is referred to the web version of this article.)

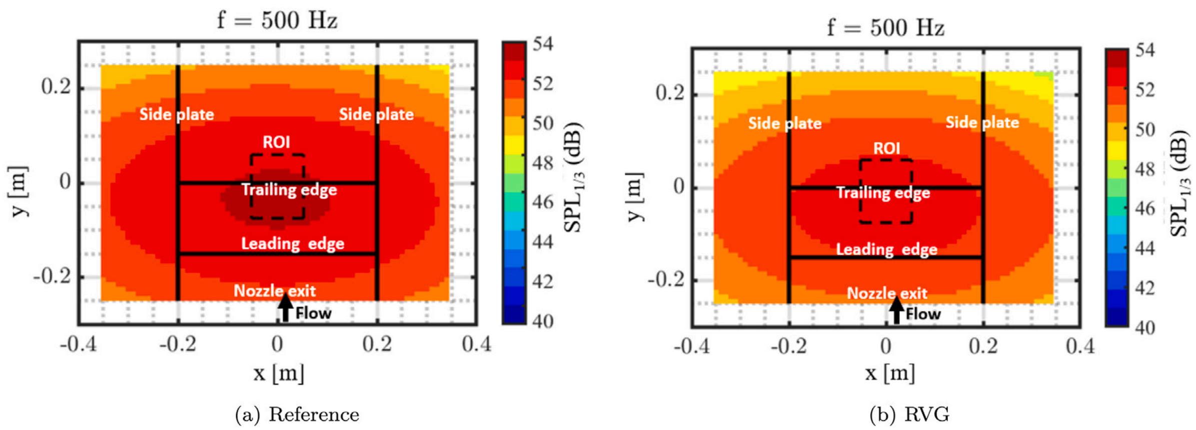

Fig. 14. Contour maps of SPL for airfoils with AoA = 6° at low frequency (500 Hz).

A qualitative analysis of the source characteristics is conducted through the contour maps. The presence of various noise sources such as trailing edge noise, leading edge noise, separation noise, noise due to side plate installation, nozzle exit noise, etc. is expected. These sources are expected to be dominant at certain frequencies. A reduction in the separation noise due to the effectiveness of RVGs is foreseen for flow controlled airfoils. The impact of the RVGs on the trailing edge noise at varying boundary layer characteristics (achieved through varying angles of attack) and at different frequencies is expected. The SPL contour maps for airfoils (forced transition) at AoA = 6° where a large turbulent separation zone extending almost up to mid-chord is observed (Fig. 8) is analyzed for a broad range of frequencies from 300 Hz to 4000 Hz.

The contour maps of SPL values at three selected frequencies are presented. A reduction of sound levels can be observed at low frequency for the airfoil with RVGs in Fig. 14. To observe the sound sources affected by the rods, contour maps of SPL are plotted at 1600 Hz (Fig. 15). Particularly, this frequency is chosen as it depicts the maximum increase in noise levels between the flow controlled and reference airfoils. Furthermore, to present the various sources, one sample frequency of 3150 Hz is chosen, and the contour maps for the reference and the RVGs airfoil is presented in Fig. 16.

The presence of several sound sources can be observed at different frequencies. Noise sources due to the side plate installation are observed in the maps at mid and high frequencies (Fig. 16). Trailing edge noise sources can be observed for a broad range of frequencies. For this particular angle, at the low frequency ranges (≤500 Hz) there is a decrease in sound levels in the flow with rods (and generated streamwise vortices) when compared to the reference foil. This reduction is observed throughout the source map (maximum of ∼1.5 dB at 400 Hz) and without discernible individual sources. This is due to the coarse resolution value of the array (3.53c) at this particular frequency (400 Hz). At lower frequencies, distinct individual noise sources cannot be distinguished on the source map due to the resolution limitation (minimum distance between the sources) of the array imposed by Rayleigh's condition (Eq. (2)). Hence, only a single large source encompassing the entire map is observable.

The rods generate more trailing edge noise at mid and high frequencies. The streamwise vortices generated by the RVGs (Fig. 10) energize the boundary layer flow by bringing in high-momentum fluid closer to the airfoil surface. This leads to increased pressure fluctuations thereby increasing the trailing edge noise. For instance, a maximum increase of ∼2 dB by the rods is observed at 1600 Hz (Fig. 15). The peak SPL value is ∼53 dB at 500 Hz.

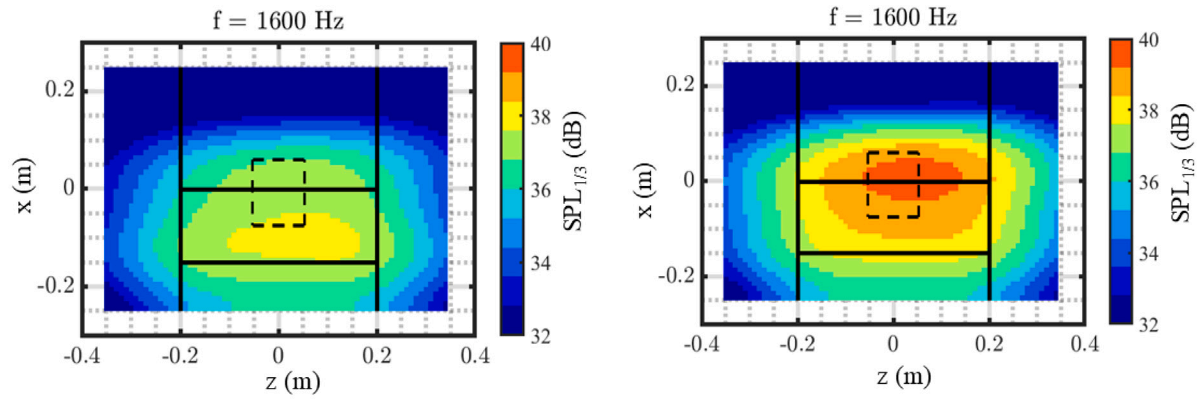

(a) Reference (b) RVG

Fig. 15. Contour maps of SPL for airfoils with AoA = 6° at mid frequency (1600 Hz).

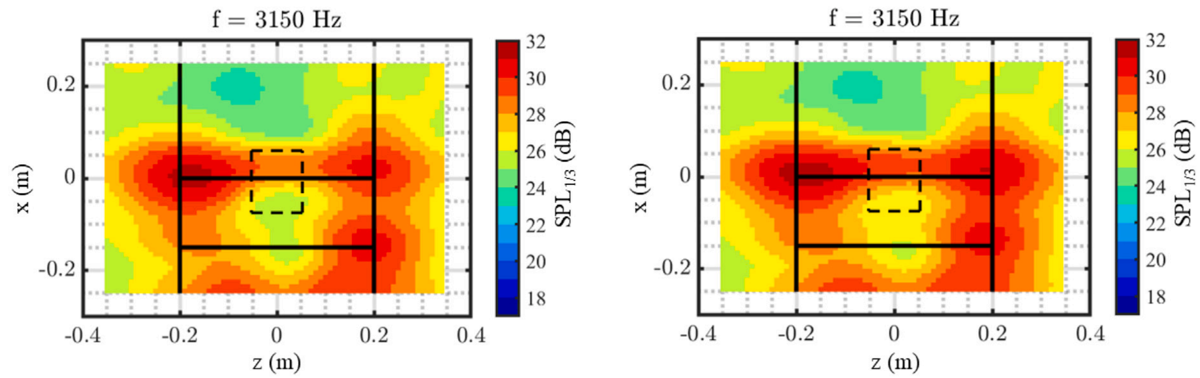

(a) Reference (b) RVG

Fig. 16. Contour maps of SPL for airfoils with AoA = 6° at high frequency (3150 Hz).

To observe the influence of increasing inflow angles (0°, 4°, 8° and 11°) on the sound levels generated by the airfoils, ΔSPL curves with respect to 0° are plotted in the ROI for the reference airfoil (Fig. 17).

SPL curves show an increase in the sound emitted with increasing inflow angles at low frequencies (<750 Hz). The peak amplitudes emitted shift to lower frequencies with increasing inflow angles. The sound pressure levels then continually decrease for the medium frequencies up to ∼1600 Hz and then increase slightly. At higher inflow angles (8°, 11°) the sound levels are lower than the low inflow angles at frequency ∼700 Hz and above.

To focus on the impact of the streamwise vortices on the trailing edge noise over a range of frequencies, the sound pressure levels integrated in the ROI (Fig. 6), are discussed below. The ΔSPL ($\mathrm{SPL}_{RVGs} - \mathrm{SPL}_{Reference}$) curves at two angles are presented in Figs. 18 and 19.

The acoustic trends are similar at both, low inflow angle of 2° (no turbulent separation) and at a high inflow angle of 6° (turbulent separation). For AoA = 2°, frequencies up to 1200 Hz, the rods decrease the emitted sound levels and above 1200 Hz, airfoil with RVGs begin to emit louder sound than the reference airfoils (Fig. 18). SPL values increase linearly until ∼2000 Hz and then for higher frequencies the values remain almost the same. For AoA = 6°, frequencies up to 700 Hz, airfoil with RVGs emit lower sound levels than the reference case, from 700 Hz to 1000 Hz, airfoil with RVGs emit linearly increasing sound levels. Above 1000 Hz, airfoil with RVGs generate more noise than reference airfoils however, the SPL difference decreases (Fig. 19). It is important to note that the increase of noise levels by the rods are all within ∼2 dB and occurs at total sound pressure levels which are significantly lower than the peak amplitudes generated at low frequencies, thus making it difficult for human perception. The overall sound pressure levels are presented in Table 4 along with their difference. The difference ΔOASPL is computed using $\mathrm{OASPL}_{RVGs} - \mathrm{OASPL}_{Reference}$.

From the table, the overall sound levels are comparable for the reference and the flow controlled cases. The impact of the rods on the OASPL values is negligible against the improved aerodynamic performance.

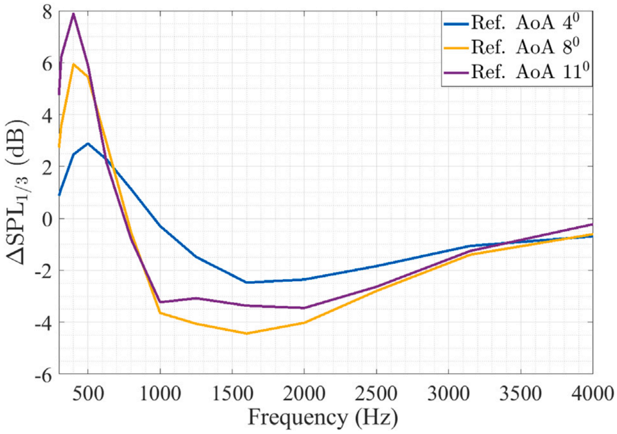

Fig. 17. ΔSPL curves for reference airfoil at various angles (ΔSPL = SPL_{AoA} - SPL_{0^0}). (For interpretation of the references to color in this figure legend, the reader is referred to the web version of this article.)

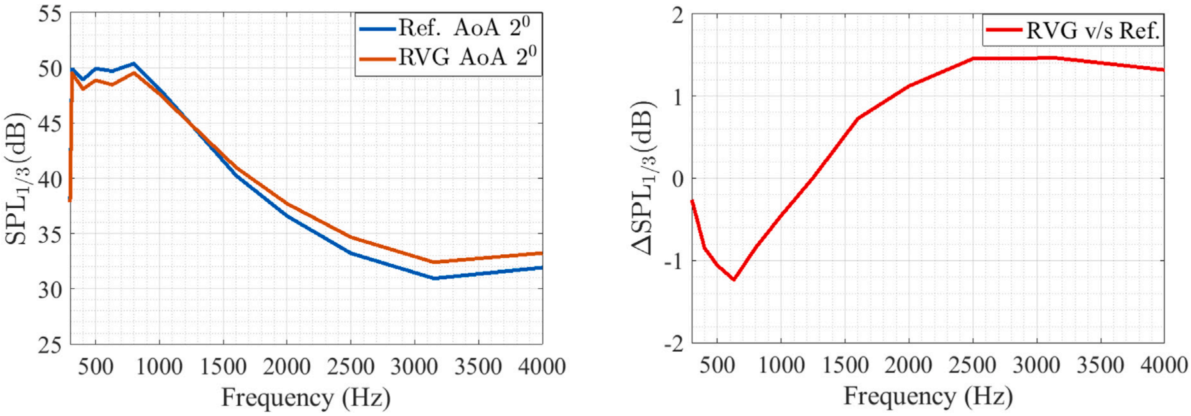

Fig. 18. SPL analysis for tripped DU96-W-180 airfoil at AoA = 2°. (For interpretation of the references to color in this figure legend, the reader is referred to the web version of this article.)

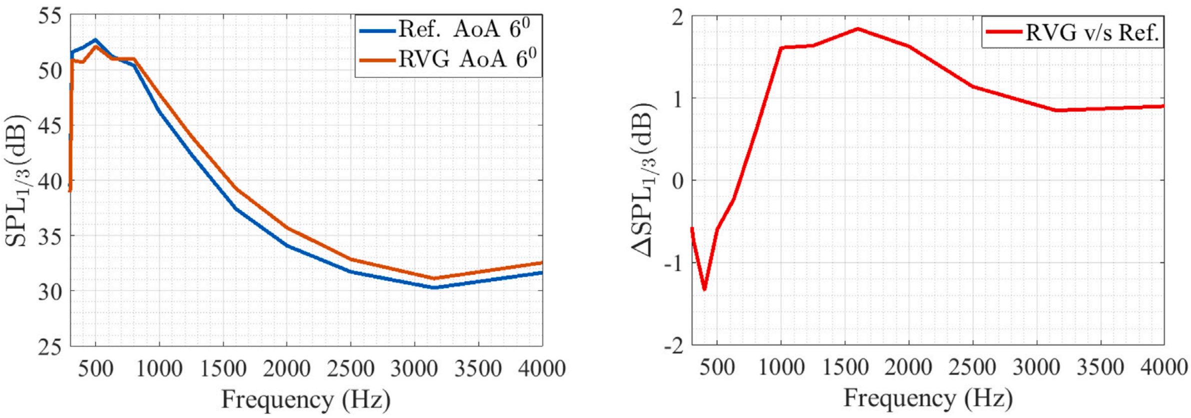

Fig. 19. SPL analysis for tripped DU96-W-180 airfoil at AoA = 6°. (For interpretation of the references to color in this figure legend, the reader is referred to the web version of this article.)

RVGs (embedded in the boundary layer) emit an additional self-noise at certain frequencies. The frequencies at which this effect is observed in the contour maps are estimated through the characteristic dimension of the RVG (H) and the acoustic wavelength

Table 4
Overall sound pressure level.

Configuration	Reference	RVG	ΔOASPL
AoA = 2°	57.7 dB	57.1 dB	−0.67 dB
AoA = 6°	59.1 dB	58.8 dB	−0.26 dB

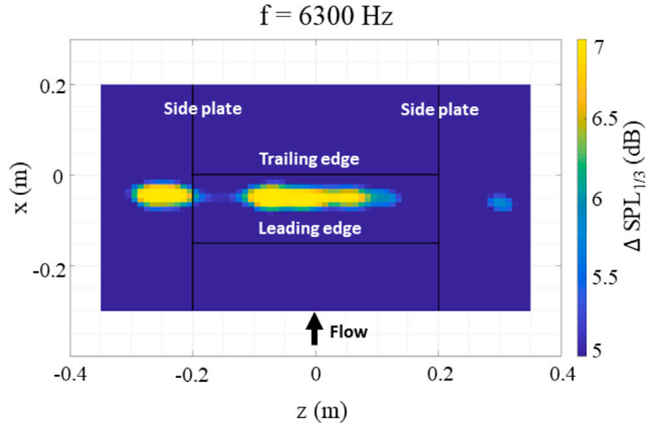

Fig. 20. Contour map of ΔSPL for airfoil with AoA = 6° at dominant frequency (6300 Hz) from CleanSC.

(λ) (Kolkman et al., 2018). The characteristic dimension of RVGs (H) computed from RVG height (h) of 2 mm and RVG skew angle (ϕ) of 30° is $H = 4$ mm. The efficiency of sound radiation increases when the turbulent eddies of the boundary layer are scattered by geometric singularities (such as RVGs). Undisturbed eddies are not effective emitters of sound. The RVG self-noise is dominant (sound scattering) when the turbulent boundary layer thickness (eddies) is proportional to the acoustic wavelength of radiated sound (Kolkman et al., 2018; Rienstra and Hirschberg, 2019).

The frequency (f) at which this occurs is determined using the Strouhal number (St). This is calculated using $St = fD/U$, with rod diameter (D) of 0.8 mm, $St \approx 0.2$ (Knisely, 1990), and approximate flow velocity (velocity inside the boundary layer is non-uniform) between the range of 15 m/s to 30 m/s ($U/2$ to U_{max}). This yields a frequency range of 3750 Hz to 7500 Hz.

With the assumption that the biggest eddies in the turbulent boundary layer are dominant (Kolkman et al., 2018), at frequencies lower than the dominant frequency, the acoustic wavelength is much larger than the eddies ($H \ll \lambda$), thus no effective distortion of the eddies takes place. Similarly, at higher frequencies than the dominant frequency, the acoustic wavelength is smaller than the eddies generated by the RVGs ($H \gg \lambda$), thus no scattering of the sound waves takes place.

The contour maps for a frequency range around the dominant frequency i.e 5623 Hz to 7079 Hz is plotted. The maps from the CBF method depict many sources including the sound sources due to the side plate installation, masking the sources due to the rods. To clean up the secondary lobes, the contour maps from the CleanSC method are presented in Fig. 20.

The contour maps exhibit the presence of rods (Fig. 20) at mid-chord. The rods generate dominant sources of self-noise rather than the trailing edge noise at high frequencies. They generate higher sound levels by ~2 dB when compared to the reference airfoil. However, the overall sound levels are quite low (26 dB) when compared to the total sound pressure levels.

5. Conclusions

The impact of specific types of vortex generators — rod type (RVGs) on the separation zone reduction and the trailing edge noise emitted by a wind turbine airfoil (DU96-W-180) is evaluated. Turbulent flow separation close to the trailing edge occurs on airfoils as the inflow angles are increased and a large separation zone extending up to mid-chord is observed after certain inflow angles. A 23% reduction in the separation zone due to the mixing of the streamwise vortices (generated by the rods) within the boundary layer is observed through oil flow visualization. The re-energizing of the boundary layer by the rods was characterized through PIV analysis. The turbulent boundary layer has been presented upstream and downstream of the RVGs, both qualitatively and quantitatively. The mean and instantaneous components of both wall-parallel and wall-normal velocity across the three planes in the spanwise direction indicate the presence of a streamwise vortex. Thus, the impact of the RVGs on the boundary layer characteristics is estimated.

Their impact on the turbulent trailing edge noise is analyzed through spectral analysis for a range of frequencies. The relative difference in the SPL and the OASPL between the reference airfoil and the airfoil equipped with the RVGs has been investigated. An increase in the overall sound pressure levels is noted for the airfoils with the flow control device if the inflow angle increases. This is anticipated since the boundary layer thickness also increases with increasing angles of attack. Similar to the triangular vane-type VGs (Kolkman et al., 2018), the RVGs also increase trailing edge noise at higher frequencies. However, they depict a decrease in the trailing edge noise at low frequencies — particularly up to 1200 Hz at angles where there is no separation and up to 700 Hz at angles where there is a large separation. Additionally, it is important to note that the relative increase in values at higher frequencies is <2 dB which is negligible (array uncertainty is ±1 dB) compared to the overall sound pressure levels. The RVG self-noise of ∼2 dB is emitted only at certain dominant frequencies estimated through the acoustic wavelength which is dependent on the boundary layer thickness. This self-noise is influenced by the characteristic dimension of the RVGs.

Similar to other classical VG types, the strength of the streamwise vortices generated by the rods is determined by their geometric dimensions and their installation location. This in turn impacts both their effectiveness in the reduction of boundary layer separation and sound emission. The impact on trailing edge noise varies with the frequency subjected to incoming flow characteristics (boundary layer thickness) influenced by the inflow velocities and angles.

In the present study, the boundary layer thickness based on which the geometric dimensions of the rods are designed was estimated from numerical simulations without the zig-zag tape. For further studies in the future, the alteration of the boundary layer characteristics through a trip tape can be included in the design process of the rods. The effectiveness of the rods in decreasing the turbulent flow separation zone depends on the strength of the streamwise vortices which is a function of the size of the rods. The influence of the strength of the vortices generated by the rods on the relative acoustic emissions by the airfoil can be studied. The present data and findings can be utilized for validation and comparison of the results obtained from the detailed numerical simulations (Large Eddy Simulations — LES) in the future. These analyses of the flow structures generated by the RVGs along with their influence on the separation and trailing edge noise emissions can be numerically investigated through LES and semi-empirical models for trailing edge noise in the future.

CRediT authorship contribution statement

Thanushree Suresh: Conceptualization, Data curation, Formal analysis, Investigation, Methodology, Resources, Validation, Visualization, Writing – original draft, Writing – review & editing. **Pawel Flaszynski:** Conceptualization, Formal analysis, Funding acquisition, Project administration, Resources, Software, Supervision, Writing – review & editing. **Alejandro Rubio Carpio:** Investigation, Methodology, Resources, Software, Supervision. **Marcin Kurowski:** Investigation, Methodology, Supervision. **Michal Piotrowicz:** Formal analysis, Investigation, Methodology, Resources, Software. **Oskar Szulc:** Conceptualization, Investigation, Software, Supervision.

Declaration of competing interest

The authors declare that they have no known competing financial interests or personal relationships that could have appeared to influence the work reported in this paper.

Data availability

Data will be made available on request.

Acknowledgments

This research was supported by the European Union's Horizon 2020 research and innovation programme under the Marie Sklodowska-Curie grant agreement No. 722401-SmartANSWER, and by the National Science Centre, Poland's funding scheme Preludium under the project No. 2022/45/N/ST8/01425 and by the CI TASK. The authors would like to thank Daniele Ragni and Christopher Teruna from Delft University of Technology for their immense support during this research work.

References

Abbott, I.H., Von Doenhoff, A.E., 2012. Theory of Wing Sections: Including a Summary of Airfoil Data. Courier Corporation.

Allen, C., Blake, W., Dougherty, R., Lynch, D., Soderman, P., Underbrink, J., 2002. Aeroacoustic Measurements. Springer, http://dx.doi.org/10.1007/978-3-662-05058-3.

Avallone, F., van der Velden, W., Ragni, D., Casalino, D., 2018. Noise reduction mechanisms of sawtooth and combed-sawtooth trailing-edge serrations. J. Fluid Mech. 848, 560–591. http://dx.doi.org/10.1017/jfm.2018.377.

Blake, W.K., Gershfeld, J.L., 1989. The Aeroacoustics of Trailing Edges. Springer Berlin Heidelberg, Berlin, H., pp. 457–532. http://dx.doi.org/10.1007/978-3-642-83831-6/10,

Bons, J.P., Rolf, S., Rivir, R.B., 2000. Turbine separation control using pulsed vortex generator jets. J. Turbomach. 123 (2), 198–206. http://dx.doi.org/10.1115/1.1350410.

Bowdler, D., Leventhall, G., Raspet, R., 2012. Wind turbine noise. J. Acoust. Soc. Am. 132, 1233. http://dx.doi.org/10.1121/1.4728202.

Brooks, T., Humphreys, W., 1999. Effect of directional array size on the measurement of airframe noise components. In: 5th AIAA/CEAS Aeroacoustics Conference and Exhibit. http://dx.doi.org/10.2514/6.1999-1958.

Cao, J.F., Zhu, W.J., Shen, W.Z., Sørensen, J.N., Sun, Z.Y., 2020. Optimizing wind energy conversion efficiency with respect to noise: A study on multi-criteria wind farm layout design. Renew. Energy 159, 468–485.

Carpio, A.R., Avallone, F., Ragni, D., 2018. On the role of the flow permeability of metal foams on trailing edge noise reduction. In: 2018 AIAA/CEAS Aeroacoustics Conference. http://dx.doi.org/10.2514/6.2018-2964.

Carpio, A.R., Martinez, R.M., Avallone, F., Ragni, D., Snellen, M., van der Zwaag, S., 2019. Experimental characterization of the turbulent boundary layer over a porous trailing edge for noise abatement. J. Sound Vib. 443, 537–558. http://dx.doi.org/10.1016/j.jsv.2018.12.010.

Chen, Z., Wen, C., 2021. Flow control of a D-shaped bluff body using different DBD plasma actuators. J. Fluids Struct. 103, 103292.

Clauser, F.H., 1956. The turbulent boundary layer. Adv. Appl. Mech. 4, 1–51.

Davies, H., Gagnon, Y., Guidotti, T., Giguere, C., Grace, S., Howe, B., Johnson, D., Persson Waye, K., Harrison, R., Roberts, J., 2015. Understanding the Evidence: Wind Turbine Noise: The Expert Panel on Wind Turbine Noise and Human Health. The Council of Canadian Academies.

De Tavernier, D., Ferreira, C., Viré, A., LeBlanc, B., Bernardy, S., 2021. Controlling dynamic stall using vortex generators on a wind turbine airfoil. Renew. Energy 172, 1194–1211.

Doerffer, P., 2014. Aerodynamic and aero-acoustic analysis of helicopter rotor blades in hover. In: Bubak, M., Kitowski, J., Wiatr, K. (Eds.), eScience on Distributed Computing Infrastructure: Achievements of PLGrid Plus Domain-Specific Services and Tools. Springer International Publishing, pp. 429–444. http://dx.doi.org/10.1007/978-3-319-10894-0/31.

Doolan, C., 2013. A review of wind turbine noise perception, annoyance and low frequency emission. Wind Eng. 37 (1), 97–104.

Flaszyński, P., Szwaba, R., 2008. Optimisation of streamwise vortex generator. Dev. Mech. Eng. 2.

Flaszynski, P., Szwaba, R., Doerffer, P., 2016. Comparison of vortex generators effect on shock wave induced separation. In: 8th AIAA Flow Control Conference, Washington D. C.. http://dx.doi.org/10.2514/6.2016-3769.

Gao, L., Zhang, H., Liu, Y., Han, S., 2015. Effects of vortex generators on a blunt trailing-edge airfoil for wind turbines. Renew. Energy 76, 303–311.

Garcia-Sagrado, A., Hynes, T., 2012. Wall pressure sources near an airfoil trailing edge under turbulent boundary layers. J. Fluids Struct. 30, 3–34.

Gardner, A., Richter, K., 2013. Effect of the model-sidewall connection for a static airfoil experiment. J. Aircr. 50, 677–680. http://dx.doi.org/10.2514/1.C032011.

Greenblatt, D., Treizer, A., Eidelman, A., Mueller-Vahl, H., 2012. Flow-control-induced vibrations for power generation using pulsed plasma actuators. J. Fluids Struct. 34, 170–189.

Gad-el Hak, M., Bushnell, D.M., 1991. Separation control: Review. J. Fluids Eng. 113 (1), 5–30. http://dx.doi.org/10.1115/1.2926497.

Hanning, C.D., Evans, A., 2012. Wind Turbine Noise. Vol. 344, Springer, http://dx.doi.org/10.1136/bmj.e1527.

Johnston, J.P., Mosier, B.P., Khan, Z.U., 2002. Vortex generating jets; effects of jet-hole inlet geometry. Int. J. Heat Fluid Flow 23 (6), 744–749.

Knisely, C.W., 1990. Strouhal numbers of rectangular cylinders at incidence: A review and new data. J. Fluids Struct. 4 (4), 371–393. http://dx.doi.org/10.1016/0889-9746(90)90137-T.

Kolkman, D., Santana, L.D., Sanders, M.P.J., Garrel, A.V., Venner, C.H., Arc, C., 2018. Experimental characterization of vortex generators induced noise of wind turbines. In: 2018 AIAA/CEAS Aeroacoustics Conference. http://dx.doi.org/10.2514/6.2018-2800.

Kösters, W., Hoerner, S., 2023. Simultaneous flow measurement and deformation tracking for passive flow control experiments involving fluid–structure interactions. J. Fluids Struct. 121, 103956.

Latoufis, K., Riziotis, V., Voutsinas, S., Hatziargyriou, N., 2019. Effects of leading edge erosion on the power performance and acoustic noise emissions of locally manufactured small wind turbine blades. J. Phys. Conf. Ser. 1222, 12010. http://dx.doi.org/10.1088/1742-6596/1222/1/012010.

Lewandowski, T., 2017. Retractable rod vortex generator. In: Doerffer, P., Barakos, G.N., Luczak, M.M. (Eds.), Recent Progress in Flow Control for Practical Flows: Results of the STADYWICO and IMESCON Projects. Springer, pp. 175–203.

Lin, J.C., 2002. Review of research on low-profile vortex generators to control boundary-layer separation. Prog. Aerosp. Sci. http://dx.doi.org/10.1016/S0376-0421(02)00010-6.

Lord Rayleigh, F.R.S., 1879. XXXI. Investigations in optics, with special reference to the spectroscope. Lond. Edinb. Dublin Philos. Mag. J. Sci. 8 (49), 261–274. http://dx.doi.org/10.1080/14786447908639684.

Luesutthiviboon, S., Malgoezar, A.M.N., Martinez, R.M., Snellen, M., Sijtsma, P., Simons, D.G., 2019. Enhanced HR-CLEAN-SC for resolving multiple closely spaced sound sources. Int. J. Aeroacoust. 18 (4–5), 392–413. http://dx.doi.org/10.1177/1475472X19852938.

Luesutthiviboon, S., Malgoezar, A., Snellen, M., Sijtsma, P., Simons, D., 2018. Improving source discrimination performance by using an optimized acoustic array and adaptive high-resolution CLEAN-SC beamforming. In: Berlin Beamforming Conference.

Martinez, R.M., Luesutthiviboon, S., Zamponi, R., Carpio, A.R., Ragni, D., Sijtsma, P., Snellen, M., Schram, C., 2020. Assessment of the accuracy of microphone array methods for aeroacoustic measurements. J. Sound Vib. 470, 115176. http://dx.doi.org/10.1016/j.jsv.2020.115176.

Merino-Martinez, R., Carpio, A.R., Pereira, L.T.L., van Herk, S., Avallone, F., Ragni, D., Kotsonis, M., 2020. Aeroacoustic design and characterization of the 3D-printed, open-jet, anechoic wind tunnel of delft university of technology. Appl. Acoust. 170, 107504.

Monir, H.E., Tadjfar, M., Bakhtian, A., 2014. Tangential synthetic jets for separation control. J. Fluids Struct. 45, 50–65.

Oerlemans, S., 2009. Detection of Aeroacoustic Sound Sources on Aircraft and Wind Turbines (Ph.D. thesis). University of Twente, Netherlands.

Oerlemans, S., Fisher, M., Maeder, T., Kogler, K., 2009. Reduction of wind turbine noise using optimized airfoils and trailing-edge serrations. AIAA J. 47 (6), 1470–1481. http://dx.doi.org/10.2514/1.38888.

Oerlemans, S., Sijtsma, P., Mendez Lopez, B., 2007. Location and quantification of noise sources on a wind turbine. J. Sound Vib. 299 (4–5), 869–883. http://dx.doi.org/10.1016/j.jsv.2006.07.032.

Padois, T., Prax, C., Valeau, V., 2013. Numerical validation of shear flow corrections for beamforming acoustic source localisation in open wind-tunnels. Appl. Acoust. 74 (4), 591–601. http://dx.doi.org/10.1016/j.apacoust.2012.09.013.

Pauley, W.R., Eaton, J.K., 1988. Experimental study of the development of longitudinal vortex pairs embedded in a turbulent boundary layer. AIAA J. 26 (7), 816–823. http://dx.doi.org/10.2514/3.9974.

Prime, Z., Doolan, C., 2013. A comparison of popular beamforming arrays. Proc. Acoust..

Puzyrewski, R., Sawicki, J., 1987. Podstawy Mechaniki Plynow i Hydrauliki. Wydawnictwo Naukowe PWN.

Rienstra, S.W., Hirschberg, A., 2019. An Introduction to Acoustics. Vol. 0103, Technische Universiteit and Version, Eindhoven.

Santana, L., 2017. Fundamentals of acoustic beamforming. NATO Sci. Technol. 1–26.

Sareen, A., Sapre, C.A., Selig, M.S., 2014. Effects of leading edge erosion on wind turbine blade performance. Wind Energy 17 (10), 1531–1542. http://dx.doi.org/10.1002/we.1649.

Sarradj, E., 2010. A fast signal subspace approach for the determination of absolute levels from phased microphone array measurements. J. Sound Vib. 329 (9), 1553–1569. http://dx.doi.org/10.1016/j.jsv.2009.11.009.

Scarano, F., 2001. Iterative image deformation methods in PIV. Meas. Sci. Technol. 13 (1), R1.

Sijtsma, P., 2010. Phased array beamforming applied to wind tunnel and fly-over tests. In: SAE Brazil International Noise and Vibration Congress. http://dx.doi.org/10.4271/2010-36-0514.

Sijtsma, P., Martinez, R.M., Malgoezar, A., Snellen, M., 2017. High-resolution CLEAN-SC: Theory and experimental validation. Int. J. Aeroacoust. 16, 274–298. http://dx.doi.org/10.1177/1475472X17713034.

Siozos-Rousoulis, L., Lacor, C., Ghorbaniasl, G., 2017. A flow control technique for noise reduction of a rod-airfoil configuration. J. Fluids Struct. 69, 293–307.

Souverein, L.J., Debiève, J.F., 2010. Effect of air jet vortex generators on a shock wave boundary layer interaction. Exp. Fluids 49 (5), 1053–1064.

Suarez, J.M., Flaszynski, P., Doerffer, P., 2018a. Application of rod vortex generators for flow separation reduction on wind turbine rotor. Wind Energy 21 (11), 1202–1215. http://dx.doi.org/10.1002/we.2224.

Suarez, J.M., Flaszynski, P., Doerffer, P., 2018b. Streamwise vortex generator for separation reduction on wind turbine rotors. Internat. J. Numer. Methods Heat Fluid Flow 28, 1047–1060.

Suryadi, A., Herr, M., 2015. Wall pressure spectra on a DU96-W-180 profile from low to pre-stall angles of attack. In: 21st AIAA/CEAS Aeroacoustic Conference, Texas. http://dx.doi.org/10.2514/6.2015-2688.

Szwaba, R., Flaszynski, P., Doerffer, P., 2019. Streamwise vortex generation by the rod. Chin. J. Aeronaut. 32 (8), 1903–1911. http://dx.doi.org/10.1016/j.cja.2019.03.033.

Tejero, F., Doerffer, P., Szulc, O., 2015. Shock wave induced flow separation control by air-jet and rod vortex generators. TASK Q.: Sci. Bull. Acad. Comput. Cent. Gdansk 19.

Tejero Embuena, F., Doerffer, P., Flaszynski, P., Szulc, O., 2018. Passive flow control application for rotorcraft in transonic conditions. Internat. J. Numer. Methods Heat Fluid Flow 28 (5), 1080–1095.

Timmer, W.A., Van Rooij, R.P.J.O.M., 2003. Summary of the delft university wind turbine dedicated airfoils. J. Sol. Energy Eng. 125 (4), 488–496.

Underbrink, J.R., 2001. Circularly symmetric, zero redundancy, planar array having broad frequency range applications.

Welch, P., 1967. The use of fast Fourier transform for the estimation of power spectra: A method based on time averaging over short, modified periodograms. IEEE Trans. Audio Electroacoust. 15, 70–73.

Westerweel, J., 1997. Fundamentals of digital particle image velocimetry. Meas. Sci. Technol. 8 (12), 1379.

Wieneke, B., 2015. PIV uncertainty quantification from correlation statistics. Meas. Sci. Technol. 26 (7), 074002.

Ye, Q., Avallone, F., Van Der Velden, W., Casalino, D., 2020. Effect of vortex generators on NREL wind turbine: aerodynamic performance and far-field noise. In: Journal of Physics: Conference Series. Vol. 1618, IOP Publishing, 052077.